ACS OMEGA

Open Access

http://pubs.acs.org/journal/acsodf

Article

Preparation of Ir/TiO_2 Composite Oxygen Evolution Catalyst and Load Analysis as Anode Catalyst Layer of Proton Exchange Membrane Water Electrolyzer

Peng Huang, Xiao Xu, Yashi Hao, Hong Zhao, Xin Liang, Zuobo Yang, Jimmy Yun, and Jie Zhang*

Cite This: *ACS Omega* 2024, 9, 34482−34492

Read Online

ACCESS | Metrics & More | Article Recommendations | Supporting Information

ABSTRACT: Electrochemical water splitting is regarded as an emerging green and sustainable hydrogen production technology because of its zero-carbon process. However, the overall cost of anode materials in a proton exchange membrane water electrolyzer (PEMWE) is high due to the use of noble metal Ir. It has been proved that introducing carrier materials to reduce the content of Ir element is a feasible cost-reduction program. Here, the Ir/TiO_2 composite material was prepared by the polyol method and used to catalyze the oxygen evolution reaction, which could effectively reduce the load amount of Ir in the membrane electrode assembly (MEA). In addition, the theoretical load of Ir was obtained by model calculation and the polarization curve test and electrochemical impedance spectroscopy (EIS) were used to discuss the relationship between Ir load in MEA and voltage loss and conductivity. The results show that MEA has lower voltage loss and better conductivity as the Ir load is in the range of 0.204−0.304 mg_{Ir}/cm^2. Altogether, an effective method to reduce the Ir load of PEMWE anode was proposed under the premise comprehensive consideration of both catalyst design and MEA preparation in this work.

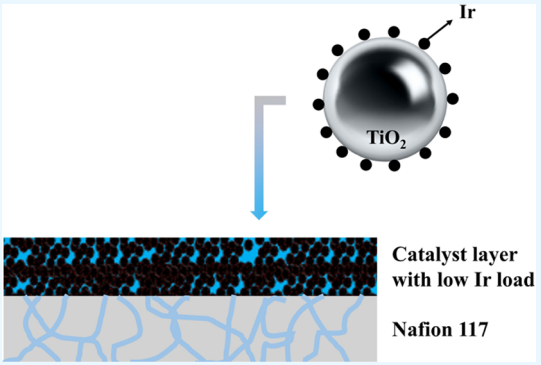

1. INTRODUCTION

With the requirement of "carbon neutral", the application of green hydrogen is regarded as a way to reduce carbon emissions and is gradually widely used.[1] At present, Ir is widely used in anodes of proton exchange membrane (PEM) water electrolyzer (PEMWE) as the preferred metal element of oxygen evolution reaction (OER) catalyst because of its superior catalytic activity and stability. Unfortunately, due to low earth surface reserve, the market price of Ir is high, making PEMWE-based hydrogen production engineering via electrochemical water splitting extremely costly.[2] Therefore, a lot of research has been carried out on highly reactive iridium-based materials and the reduction of iridium content.[3−5] One feasible method is to combine a small amount of precious metal material with other carriers to reduce the noble metal load and the process cost. High dispersion of particles is an important prerequisite for the preparation of catalysts with low Ir loading. Li's group[6] successfully reduced the average size of Ir nanodots and improved the dispersion by using the unique interlayer nanopore structure of the two-carbon substrate composed of reduced graphene oxide and sulfur-doped carbon. Similarly, in the research of Zhang et al.,[7] TiN carrier and Ir precursor were dispersed in isopropanol and water and reacted at a low temperature under the protection of nitrogen. After the reaction, IrO_2/TiN was obtained by acid pickling, drying, and calcination in air.

The design of composite catalysts based on Ir elements should focus on the selection of carrier materials. Ir-based active substances need to be highly dispersed on the surface of carrier to form a wide range of active sites to ensure acceptable catalytic activity.[8] On the other hand, as the OER catalysts are applied to PEMWE anodes, the carrier materials need to have excellent acid resistance and oxidation resistance at high potential.[9] Previous studies have used carbon materials as usual substrates due to their high specific surface area and strong metal−support interaction.[10,11] However, carbon begins to oxidize at 1.8 V and undergoes obvious corrosion at 2.0 V in a low-pH environment.[12,13] These factors lead to the lack of long-term working capacity of the catalyst layer (CL) composed of carbon materials. Unfortunately, most metal-based carriers exhibit similar unstable properties to carbon materials.[3] Using TiO_2 as the carrier is a promising pathway because its passivation effect can provide chemical protection for the devices over a wide pH range, significantly increasing the operating life of the membrane electrode assembly

Received: March 8, 2024
Revised: June 27, 2024
Accepted: June 28, 2024
Published: July 31, 2024

(MEA).[14,15] Although the electronic conductivity of this semiconductor material is low, TiO_2 particles or atomic layer deposition with appropriate size (2 nm) are prone to electron tunneling, thereby reducing the conductivity problem.[16] It has been shown that core−shell materials composed of titanium and iridium oxides can exhibit acceptable properties in proton exchange membrane electrolysis in relevant research.[17] Therefore, the trade-off between activity and stability should be considered carefully when using TiO_2 as the carrier.

In the previous theoretical research and engineering practice, the Ir load of anode CL of PEMWE was roughly in the range of 2−3 mg_{Ir}/cm^2, while using composite materials could reduce the Ir load to less than 0.5 mg_{Ir}/cm^2.[18] However, the hydrogen production efficiency of PEMWE using composite materials did not necessarily show a significant decrease, indicating that the relationship between Ir load and MEA performance was not linear.[19] The reasons for the above phenomena can be classified as follows:[20−22] (1) The combination with the carrier can change the electronic state of the active substances and then form new proton transport channels and improve the number of active sites. (2) CL is formed after the composite materials are loaded on the membrane surface, and the particle size, distribution density, and layer thickness can significantly affect the mass transfer process. (3) Under long-term operating conditions, it is usually accompanied by the precipitation and fall of surface oxygen evolution materials, resulting in a dynamic change of MEA's output performance. It can be seen that the study of anode Ir load content in MEA is a very important part as well. Although there have been works on the relationship between material factors such as metal valence[23] and micromorphology[24] and the Ir load in Ir−TiO_2 composite catalysts, reports on the effect of Ir load on the actual output performance of MEA are very rare, which is one of the main problems faced by PEMWE to achieve large-scale industrialization.

Herein, Ir/TiO_2 was prepared using the polyol method and the optimal loading in MEA was discussed. TiO_2 carrier particles were uniformly dispersed in the solution with ethylene glycol as the reducing agent, and then the Ir precursor was dispersed as well. After the reaction, acid washing was carried out to improve their activity, and the subsequent phase characterization was carried out to determine the role of different crystalline carriers in the oxygen evolution process. The addition of composite material as the oxygen evolution catalyst to MEA could reduce the amount of Ir used while ensuring hydrogen production efficiency, thus reducing the process cost. Meanwhile, the relationship between the loading of Ir element and performance in a single cell was determined, and voltage loss and electrochemical impedance spectroscopy (EIS) analysis were performed to explain the loading range under optimal activity.

2. RESULTS AND DISCUSSION

First, the physical properties of two different common crystal types of TiO_2, anatase (1-TiO_2) and rutile (2-TiO_2), were compared. As shown in Table 1, there are differences in specific surface area and nanoparticle size between different crystal types, which significantly affects the surface structure of Ir/TiO_2 and the catalytic layer thickness of MEA anode with the same Ir load. Ir/TiO_2 was prepared by the polyol method, and its morphology and particle size were analyzed by transmission electron microscopy (TEM). As shown in Figure 1a,b, the particle sizes of 1-TiO_2 and 2-TiO_2 with Ir nanoparticles are 1.984 and 2.059 nm, respectively, and their distribution range is about 0.5 nm. It can be seen that Ir and Ti are evenly distributed from elemental mapping images (Figure 1c,d). Notably, the content of Ir for 1-TiO_2 shown in energy-dispersive X-ray (EDX) spectroscopy (Figure 1e,f) is lower, which is caused by the relatively low specific surface area of 1-TiO_2. On the other hand, the basicity of rutile is relatively stronger than that of anatase, and consequently, Ir can be uniformly dispersed on 1-TiO_2, forming a large specific surface area. The Ir adsorbed on the surface of 2-TiO_2 is easy to accumulate, resulting in a specific surface area lower than Ir/1-TiO_2 after loading.[25]

Table 1. Comparison of the Physical Properties of 1-TiO_2 and 2-TiO_2

physical properties	1-TiO_2	2-TiO_2
hydrophilia	oleophilic	hydrophilic
crystal structure	100% anatase	100% rutile
carrier specific surface area (m^2/g)	32.78	41.34
specific surface area after Ir loading (m^2/g)	105.14	56.60

X-ray powder diffraction (XRD) analysis was used to determine the phase composition and crystal state of the material. As shown in Figure 2a, both materials before calcination only show the diffraction peaks of TiO_2, while without the peaks of Ir phase, indicating that the Ir element exists in the form of amorphous state. In order to determine whether the iridium species generated was the metal element or oxide, the crystal growth experiment was performed by injecting nitrogen into a tube furnace and heated to 500 °C. It can be observed that the characteristic peaks of Ir appear at 40.796° (111), 47.568° (200), 68.997° (220), and 84.105° (311) in Figure 2b after calcination. The above results can confirm that the prepared material is Ir/TiO_2. In order to further determine the structure and composition of the material, the material was characterized by high-resolution TEM (HRTEM) (Figure S1). The results show that the crystal lattices of two different types of TiO_2 are displayed in the center of the particles, respectively, while the crystal lattices displayed at the edge of the particles belong to the Ir phase, and the lattice types are consistent with the XRD patterns, which confirm that the material is TiO_2 particle with Ir on the external surface supported Ir from another point of view.

X-ray photoelectron spectroscopy (XPS) was used to analyze the elemental composition and electronic states. The results in Figure 3a show that Ti, O, and Ir elements exist in both materials, which echo the EDX results and reconfirm the successful loading of Ir species on the TiO_2 substrate. Moreover, Ti $2p_{1/2}$ peak (465.09 eV) and Ti $2p_{3/2}$ peak (459.35 eV) of Ir/2-TiO_2 shift to higher binding energy compared with Ir/1-TiO_2 (464.77 and 459.00 eV) (Figure 3b). The above evidence indicated that Ti^{4+} experienced an increase in valence state and loss of electrons.[26] The reason for these phenomena is the introduction of Ir species. Since the particle size of Ir/TiO_2 is mostly distributed near 2 nm, electron tunneling is easy to occur, resulting in strong electron exchange between the two phases after the surface loading of Ir species. Because of the better carrying capacity of Ir particles, the orbital peaks of Ir/2-TiO_2 have a higher binding energy than Ir/1-TiO_2.

Figure 3c exhibits high-resolution Ir 4f XPS spectra of Ir/1-TiO_2 and Ir/2-TiO_2. From the figure and Table 2, it can be found that the binding energy of Ir species of Ir/2-TiO_2 is

https://doi.org/10.1021/acsomega.4c02299
ACS Omega 2024, 9, 34482−34492

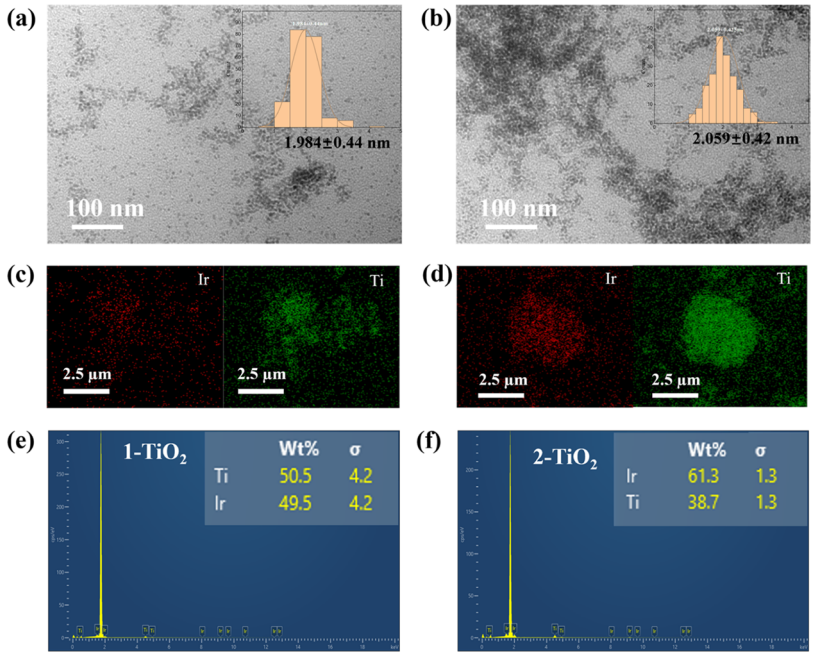

Figure 1. TEM images of Ir/1-TiO_2 (a) and Ir/2-TiO_2 (b), elemental mapping images of Ir/1-TiO_2 (c) and Ir/2-TiO_2 (d), and EDX spectrum of Ir/1-TiO_2 (e) and Ir/2-TiO_2 (f).

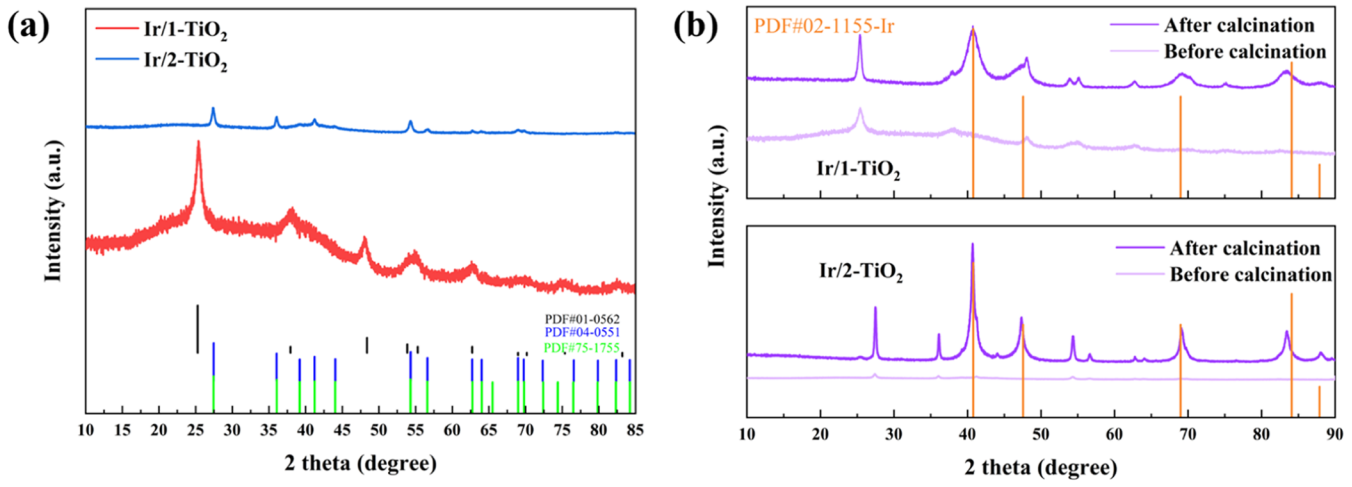

Figure 2. XRD patterns of Ir/1-TiO_2 and Ir/2-TiO_2 (a) and samples before and after calcination (b).

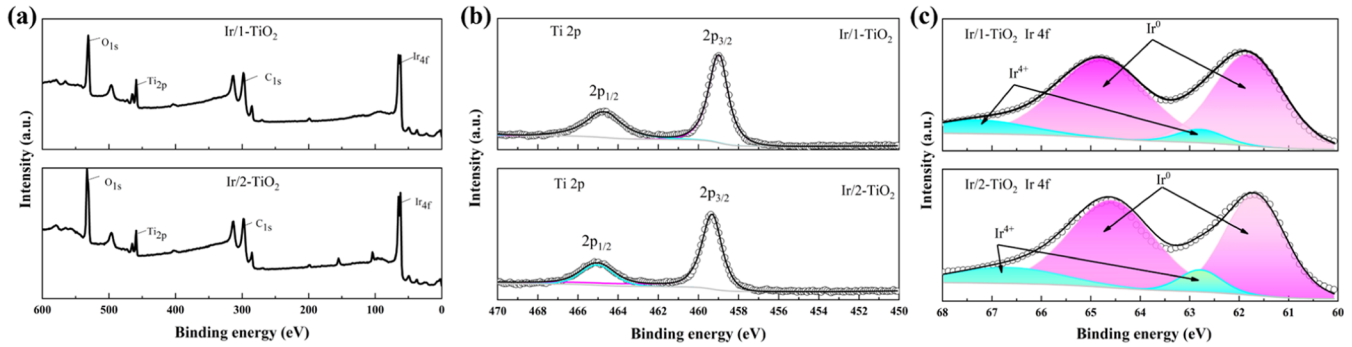

Figure 3. Survey XPS spectra of Ir/1-TiO_2 and Ir/2-TiO_2 (a); high-resolution XPS Cu 2p spectrum (b) and Ir 4f spectrum (c) of Ir/1-TiO_2 and Ir/2-TiO_2.

slightly lower than that of Ir/1-TiO_2, which is consistent with the electron transfer theory mentioned above. Since Ir/2-TiO_2 is loaded with a larger amount of Ir particles, more electrons are transferred from the TiO_2 phase to the Ir phase. Notably, the materials contain Ir species with two different valences, namely, metallic Ir (Ir^0) and oxidized Ir (Ir^{4+}). It suggests that

https://doi.org/10.1021/acsomega.4c02299
ACS Omega 2024, 9, 34482−34492

Table 2. Summary of Ir 4f Binding Energies and Peak Area Ratios of Different Crystal Types of TiO_2

samples	Ir^0 (eV)	Ir^{4+} (eV)	Ir^{4+}/Ir^0
1-TiO_2	61.88	62.78	0.142138
	64.88	67.28	
2-TiO_2	61.78	62.78	0.198128
	64.78	66.68	

some Ir particles were oxidized to hypervalent oxides (IrO_x) or bonded to hydroxyl groups ($Ir(OH)_x$), and the production of these components may alter the catalytic process of the materials.[27] By calculating the relative intensity area of Ir^0 and Ir^{4+} orbital peaks, the content proportions of high-valence Ir in the two materials were compared. The calculation results show that Ir/2-TiO_2 contains a higher proportion of high-valence Ir.

The oxygen evolution performance was analyzed by electrochemical analysis technology. First, the electrocatalytic performance of prepared materials was evaluated by the linear scan voltammogram (LSV). Figure 4a shows the LSV curves of the two materials. The curves suggest that Ir/1-TiO_2 has better catalytic oxygen evolution activity when the oxidation potential is applied. For Ir/1-TiO_2, the drive overpotentials required to reach 10 and 50 current density are 288 and 346 mV, respectively, significantly lower than that required for Ir/2-TiO_2 (308 and 375 mV) (Figure 4b). Meanwhile, Figure 4c shows the Tafel plots of newly prepared materials that are used to study their influence on the OER mechanism. Generally, materials with low Tafel slope values have more efficient catalytic kinetics, making the reaction easier to proceed. The Tafel slopes of Ir/1-TiO_2 and Ir/2-TiO_2 were calculated to be 54.4 and 57.7 mV/dec respectively. As expected, Ir/1-TiO_2 exhibits a lower Tafel slope value, indicating high OER activity and fast catalytic kinetics. Figure 4d shows a comparison of the mass activity of different materials. The oxygen evolution performances of the unit active substance in catalytic materials were evaluated by the mass specific activity. At a voltage of 1.5 V, 1-TiO_2 and 2-TiO_2 can reach 240.13 and 30.76 mA/mg_{Ir}, respectively, which means that the mass activity of 1-TiO_2 is higher and can reach 7.81 times of 2-TiO_2. The primary reason is the difference in specific surface area between the two materials. According to Table 1, although the specific surface area of 2-TiO_2 as the carrier is larger, the opposite result appears after loading Ir, which is favorable for the active substance in Ir/1-TiO_2 to expose more active sites.[28] Therefore, the Ir component in Ir/1-TiO_2 has higher catalytic mass specific activity.

In the potential range of the electrochemical oxygen evolution reaction, the electrochemically active area can be characterized by the voltammetry analysis so as to evaluate the number of active sites involved in the reaction (the specific calculation process is shown in the Supporting Information). Figure 5 and Table 3 summarize the variation rules of electric quantity and sweep speed. Due to the different carriers, the morphology of catalytic materials coated on the surface of rotating disk electrode (RDE) was various, which led to the difference in the number of active sites and the total charge carried on the electrode during the test. It could be seen that the surface electricity (Q_t) of Ir/1-TiO_2 was larger. But for the

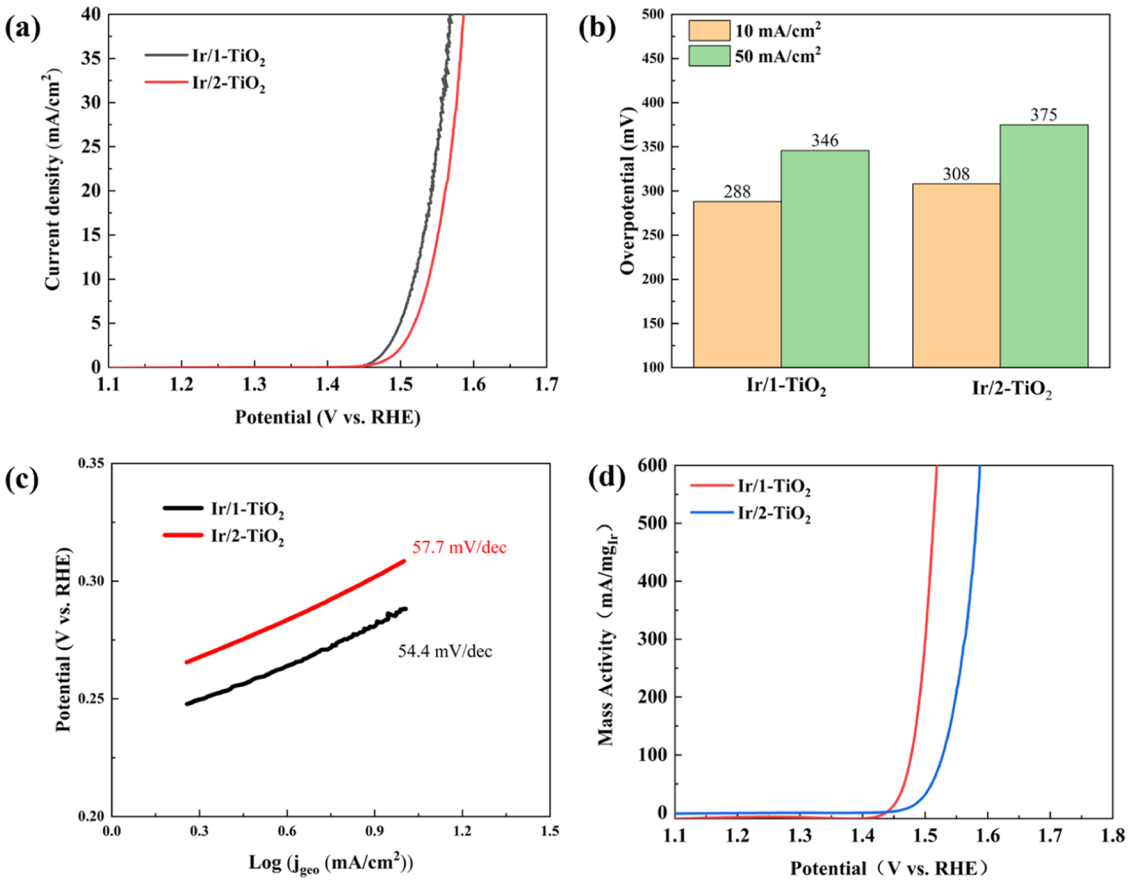

Figure 4. LSV curves (a), overpotentials at 10 and 50 mA/cm^2 (b), Tafel slopes (c), and mass activity of Ir/1-TiO_2 and Ir/2-TiO_2 (d).

https://doi.org/10.1021/acsomega.4c02299
ACS Omega 2024, 9, 34482−34492

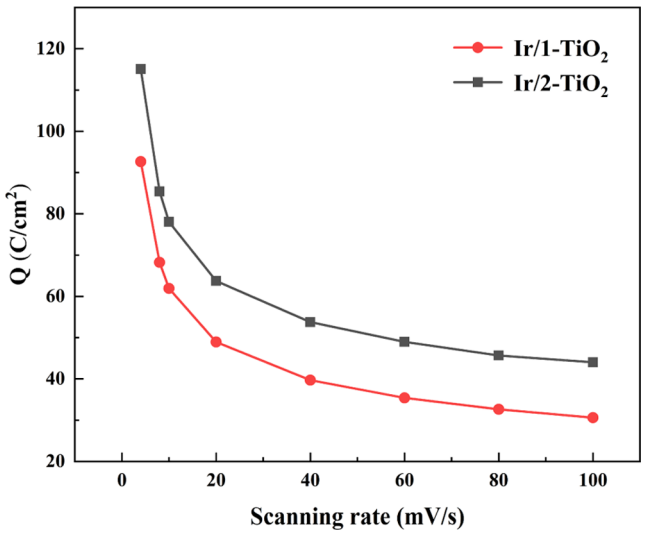

Figure 5. Electric quantity of Ir/1-TiO_2 and Ir/2-TiO_2 with different scanning rates.

Table 3. Summary of the Values of Electric Quantity

	Ir/1-TiO_2	Ir/2-TiO_2
Q_0 (C/cm^2)	526.3158	625
Q_t (C/cm^2)	42.436	27.315
Q_t/Q_0	0.08063	0.043704

total electricity (Q_0), Ir/2-TiO_2 had a higher value, which indicated that the catalytic layer formed by Ir/2-TiO_2 on RDE was thicker. Meanwhile, a larger amount of catalytic surface sites (Q_t/Q_0) reveals that the catalytic material formed by the support of 1-TiO_2 was more conducive to the catalytic oxygen evolution reaction.

PEM cell is the main place where the whole water electrolytic reaction takes place. The electrochemical process in the cell mainly takes place at the anode and cathode. The voltage in the test of electrolytic cell is the consumption in the actual electrolytic process. To reduce the energy loss in the electrolytic process, the actual operating voltage must be reduced while ensuring the activity. The reversible voltage loss, kinetic process loss, mass transfer and diffusion process loss, material resistance, and contact resistance loss coexist in the operation of PEMWE.[29,30] It is meaningful to analyze the various processes existing in the actual operation process and find the optimization way. Equations S3−S7 detail the voltage composition.

In the application of Ir matrix composites for anode, basic requirements for catalytic materials are claimed as follows:[18,31] (I) It is required to reduce the application amount (>2.0 V) of transition metals. In addition to the cost factor, the high transition metal load at a high potential will limit the ion conduction between CL and proton exchange membrane. (II) Low iridium load and excellent heap volume porosity require good transmission and diffusion channels. (III) The thickness of the catalytic layer needs to be appropriate (maintained at about 10 μm). If the thickness is much larger than this value, the proton exchange channel is too long, thus increasing the resistance. This situation is easy to lead to a high proton transmission loss voltage. On the contrary, too low thickness will make the formed channel have an adverse effect on long-term proton exchange, easily resulting in the dissolution of the catalytic material and the deactivation of the water transport functional group on the membrane surface.[32]

Before calculating the theoretical load, some necessary fact premises are presented here:

(1) The filling density of commercial TiO_2 is lower than that of Ir.
(2) The molecular weight of iridium material deposited on the TiO_2 carrier is close to the Ir molecular weight.
(3) The size of the TiO_2 carrier is much smaller than the thickness of the anode catalytic layer.
(4) Ir/TiO_2 is uniformly distributed on the membrane surface.

Based on the above premises, we calculated the theoretical load by monolayer adsorption hypothesis (Figure S2). First, the thickness of the Ir layer deposited on the surface is as follows

$$t_{Ir} = volume_{Ir}/area_{TiO_2} = (m_{Ir}/\rho_{Ir})/(m_{TiO_2} \times BET_{TiO_2}) = wt\ \%_{Ir}/(100\% - wt\ \%_{Ir}) \times (1/\rho_{Ir} \times BET_{TiO_2}) \quad (1)$$

where m_{Ir} and m_{TiO_2} are the masses of Ir and TiO_2, respectively; wt $\%_{Ir}$ is the mass fraction of Ir in the catalytic material; and the molar mass of Ir is M_{Ir} = 192 g/mol. For the prepared catalytic material, the supported Ir layer thickness t_{Ir} is about 8 nm. Then, the loading capacity of titanium dioxide is as follows

$$L_{TiO_2} = \rho_{TiO_2\text{-packing}} \times t_{electrode} \quad (2)$$

Using the aforementioned TiO_2 filling density, the loading capacity of TiO_2 can be calculated ($L_{TiO_2} \approx 1.475$ mg$_{TiO_2}$/cm^2).

According to the above, t_{Ir} is the actual iridium layer thickness supported on TiO_2, then the final load of Ir supported on the film electrode can be calculated as follows

$$L_{Ir} = L_{TiO_2} \times BET_{TiO_2} \times t_{Ir} \times \rho_{Ir} \times M_{Ir} \quad (3)$$

BET_{TiO_2} and t_{Ir} can be obtained from Figure S3 and eqs S9, and calculations based on the current analytical data show that $L_{Ir} \approx 0.278$ mg$_{Ir}$/cm^2.

The polarization curve in a single cell was determined according to Bender's method.[33] Figure 6 shows the voltage loss distribution of a single cell with different anode Ir loads of the catalytic material prepared by 1-TiO_2, and the specific analysis of different voltage losses is given in Figure 7. It can be seen in Figure 7a that ohmic loss occupies a small part (<0.078 V) because its own value is determined after assembly and conforms to Ohm's law in the whole process. It has a linear relationship with current density. However, kinetic loss (Figure 7b) occupies a large part of the loss when electrolytic water reaction occurs (>1.42 V) and does not increase significantly with the increase of current density. Mass transfer voltage loss is small at the beginning of water electrolysis (≈0 mV), and it increases linearly with the increase of current density (0−1.6 A/cm^2) (Figure 7c). Since the ionomer content is a fixed value in the preparation of MEA, its effect is not discussed here.[34] When the load is 0.454 and 0.104 mg$_{Ir}$/cm^2, the mass transfer loss voltage increases obviously at the current density (>1.6 A/cm^2). We attribute this voltage loss to the carbon corrosion in the porous transport layer (PTL). The appearance of carbon corrosion is due to the surface oxidation reaction of TGP-H-60 carbon paper under a high voltage (>2 V). Although the

https://doi.org/10.1021/acsomega.4c02299
ACS Omega 2024, 9, 34482−34492

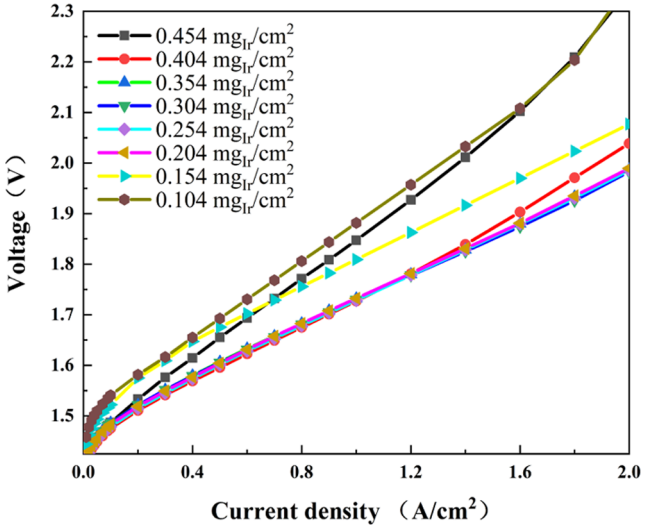

Figure 6. Single-cell polarization curves of Ir/1-TiO_2 and Ir/2-TiO_2.

voltage exceeded 2 V under 0.404 and 0.154 mg_{Ir}/cm^2, the retention time was only maintained for 5−10 min, thus the voltage was kept near 2 V.

The above phenomenon indicates that the voltage loss is the largest with the load of 0.104 and 0.454 mg_{Ir}/cm^2, while the polarization curve difference is small when the load is 0.204 and 0.354 mg_{Ir}/cm^2, indicating that the thickness of CL is not a decisive factor for the performance in a certain load range. At this point, determining the pore structure and thickness, it is the oxygen evolution activity that must be considered.

The direct theoretical basis of kinetic loss voltage is Tafel, that is, the initial voltage value of the actual electrolytic water oxygen evolution reaction or its intrinsic activity, which is positively correlated with the number of active sites on the surface of CL. It can be seen from Figure 7b that between 0.204 and 0.454 mg_{Ir}/cm^2, the kinetic loss voltage is concentrated between 0.325 and 0.348 V because Ir content can be maintained at least 5 μm thickness in this interval to maintain long-term performance, that is, the number of active sites on the surface does not change much, but is lower than 0.204 mg_{Ir}/cm^2, resulting in insufficient catalytic active sites on the surface of MEA and short mass transfer channel. It is easy for the activation (1 A/cm^2) to lead to the transition of Ir in the surface CL to IrO_2 or an even higher price state. Moreover, due to the shortening of the transmission channel, the phenomenon of hydrogen in oxygen and oxygen in hydrogen exists in the anode, which is more obvious with the increase of voltage. Meanwhile, the phenomenon of material maturation under high voltage is more specific. The reduction of ion transport channels is not enough to support the long-term oxygen evolution process on the CL surface. The significant decrease of the active sites on the surface results in a decrease in the activity of the material when the oxygen evolution reaction occurs.

According to the analysis of voltage loss caused by mass transfer diffusion, as shown in Figure 7c, it can be obviously observed that the voltage loss is the minimum at 0.304 mg_{Ir}/

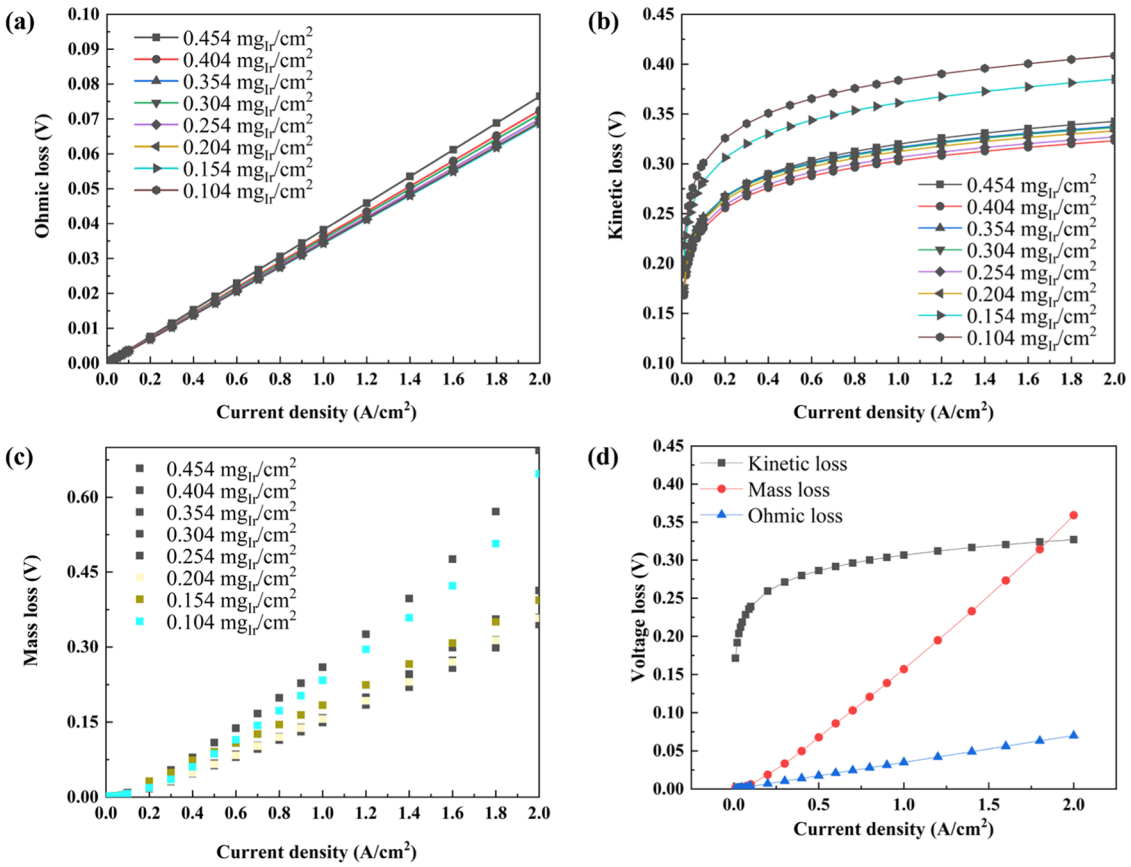

Figure 7. Voltage loss analysis of ohmic loss (a), kinetic loss (b), and mass loss (c) of MEA with different Ir/1-TiO_2 loads, and voltage loss comparison of MEA with 0.254 mg_{Ir}/cm^2 Ir/1-TiO_2 load (d).

https://doi.org/10.1021/acsomega.4c02299
ACS Omega 2024, 9, 34482−34492

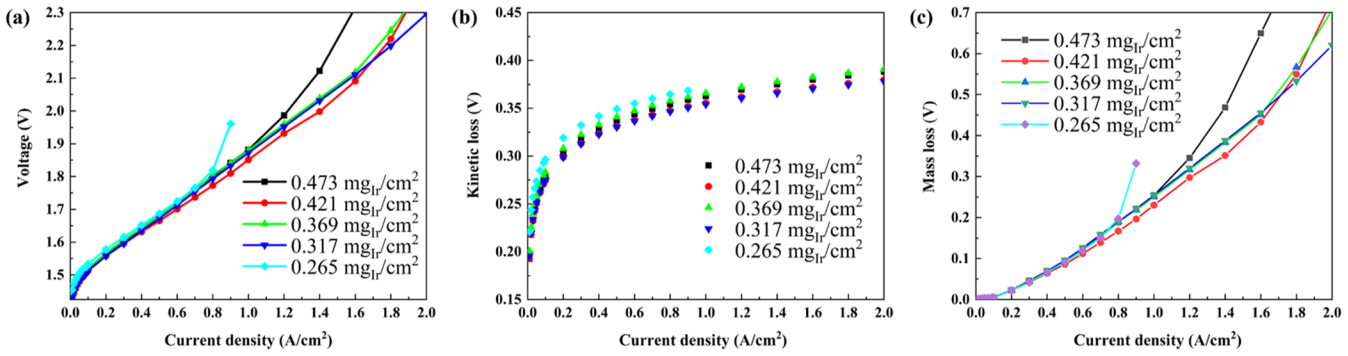

Figure 8. Single-cell polarization curves (a) and the voltage loss analysis of kinetic loss (b) and mass loss (c) of MEA with different Ir/2-TiO_2 loads.

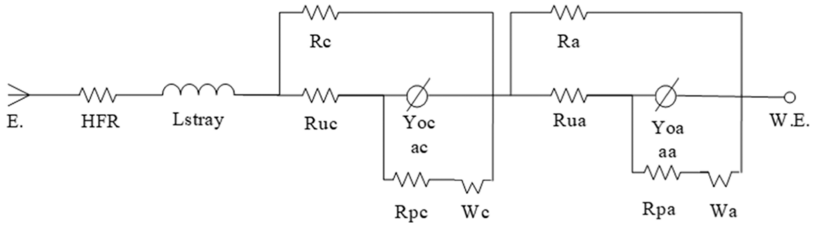

Figure 9. Equivalent circuit diagram for impedance fitting.

cm^2, and its loss at the full current density presents a V-shaped trend, that is, mass transfer diffusion loss decreases first and then increases with the decrease of load. This is because there is an optimal length distribution of the gas−liquid diffusion channel in CL, and the width of the gas−liquid transmission channel is also consistent under the condition that the reactor density of the catalytic material is the same. The theoretical calculation and experimental verification of the above-mentioned loads showed that our calculation was valid.

It can be seen from Figure 7d that in the whole loss voltage distribution diagram, the kinetic loss process occupying the main loss is mainly attributed to the catalytic material. Therefore, in terms of reducing energy loss, the catalytic oxygen evolution material is mainly considered. The diffusion loss is mainly determined by the oxygen transport resistance of PTL at different current densities, which increases with the increase of current density (oxygen increase). Although the contact resistance occupies only a small part, it is also positively correlated with the current density. In addition, we also carried out the above experiments for Ir/2-TiO_2. The results shown in Figure 8 suggest that the above assumptions and conclusions are correct. Additionally, a chronopotentiometry test was performed on two catalysts and the MEA prepared by them. The test results show that the performance of each material and MEA does not decrease significantly during 24 h long working time, indicating that the two catalysts have considerable stability (Figure S4).

In the research of water electrolysis materials and electrolyzers, electrochemical impedance spectroscopy is a necessary analytical and characterization method. For oxygen evolution catalysts used in water electrolysis, there is an important relationship between their electrical conductivity and the ability to overcome the four-electron transfer process and the resulting voltage loss.[35−37] Moreover, the process of interfacial charge transfer is also included in external circuit electron transfer, intrinsic kinetic activation, and oxygen diffusion on the surface of the catalytic material.[5,38] The application in electrolyzer is more complex, needing to consider not only the characteristics of oxygen evolution material but also the spatial position and contact of MEA, PTL, and bipolar plate assembly.[39,40] In this process, it is first necessary to investigate the conductivity of MEA and PTL, which is divided into two parts, including proton conductivity and electron conductivity. Among them, proton conductivity is mainly related to the content of ionomers in the catalytic layer, proton exchange membrane, and thickness of the catalytic layer. The electronic conductivity is related to the physical conductivity of the material, the conductivity of the PTL, and the material of the bipolar plate.[41] The resistance impedance will inevitably lead to a certain voltage loss, and the main losses in the electrolyzer usually exist in the kinetic loss and mass transfer loss. Kinetic loss is mainly related to the oxygen evolution material, while mass transfer loss is closely related to the transport channels constructed by CL and PTL.

Figure 9 exhibits the equivalent circuit diagram, and the EIS analysis technology was used to analyze the fitting circuit of the electrolyzer. In the high-frequency impedance part (for the analysis of the Nyquist plots of the experiment, the high frequency was defined as the part larger than 100 kHz), we introduced HFR electronic components as the high-frequency resistance. Meanwhile, the inductance element Lstray was used to simulate the inductance generated by the direct current (DC) power supply in the external circuit.[42] In addition, since the contact resistance was not negligible, the resistance element R was used to simulate it in this paper.[43] When electrochemical oxygen evolution occurs, there is charge transfer, surface capacitance, ion transport, and gas (O_2, H_2) diffusion on the surface of CL.[44,45] Therefore, we used electronic components R, constant-phase element (CPE), $Warburg_s$, and $Warburg_o$ to simulate it. The ion resistance of protons passing through the Nafion 117 membrane was consistent with the resistance of the external circuit; thus, it was normalized to HFR. At high frequencies, the effect of Warburg diffusion is small, while Warburg diffusion is mainly

https://doi.org/10.1021/acsomega.4c02299
ACS Omega 2024, 9, 34482−34492

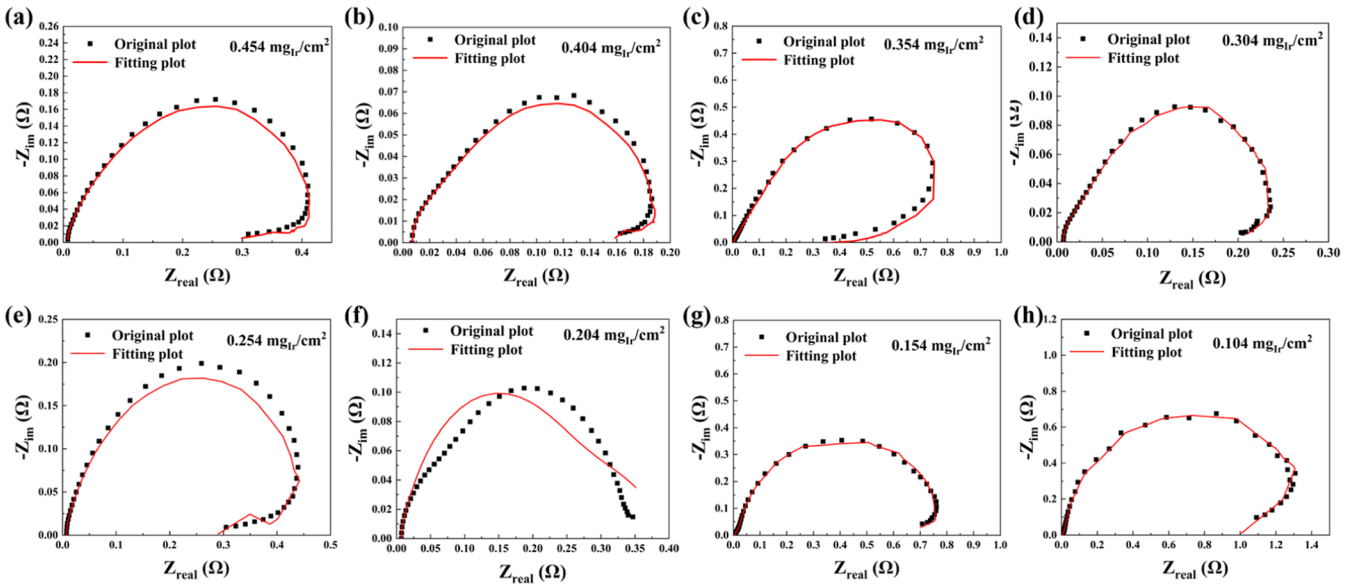

Figure 10. EIS and fitting Nyquist plots of MEA with Ir/1-TiO_2 load from 0.454 mg_{Ir}/cm^2 (a) to 0.104 mg_{Ir}/cm^2 (h).

Table 4. Values of EIS Components after Fitting

	R_a (Ω)	R_{ua} (Ω)	Y_{oa} (S s^a)	R_{pa} (Ω)	W_a (S $s^{1/2}$)
0.454 mg_{Ir}/cm^2	1.041	−0.9009	0.0496	0.0146	0.7141
0.404 mg_{Ir}/cm^2	0.4139	0.0494	0.00007	−0.0200	0.1475
0.354 mg_{Ir}/cm^2	0.4587	−0.0031	0.0315	0.00148	−2.158
0.304 mg_{Ir}/cm^2	0.09605	−0.0542	0.0262	−0.0058	2.144
0.254 mg_{Ir}/cm^2	0.1243	−0.0136	0.0356	−0.0046	0.0264
0.204 mg_{Ir}/cm^2	0.0864	−0.0154	0.0446	0.0056	0.0348
0.154 mg_{Ir}/cm^2	0.7149	−0.0105	0.0453	0.4431	0.0425
0.104 mg_{Ir}/cm^2	1.343	−0.0035	0.0283	0.5596	0.0175

controlled by oxygen diffusion time and oxygen delivery resistance in the low-frequency region (<100 Hz). Therefore, the Warburg diffusion impedance was used to evaluate the oxygen transport process in PTL and analysis at a high current density (>1 A/cm^2).[46]

We have fitted the impedance of electrolytic cells with different loads, and the goodness of fit of the data obtained by the fitted model is 0.01 ± 5%, which is an acceptable fit. Figure 10 shows that the equivalent circuit diagram is effective and can well fit the low-frequency mass transfer diffusion and kinetic reaction process. As shown in Table 4, the specific values of different components were analyzed and summarized. It can be clearly known from the table that the anodized polarization resistance (R_{pa}) of the membrane electrode changed less in the range of 0.203−0.353 mg_{Ir}/cm^2 (5‰), while the change of anode conductance (Y_{oa}) is 5%. With the gradual decrease of Ir loading, it can be found that the contact resistance (R_a) shows the same change trend as diffusion loss, which is V-shaped. The above evidence corroborates the previous conclusion, which indicates that the loading has little effect on the electrochemically active surface of the material. However, the value of R_a varies greatly with different loading, especially at 0.453 and 0.104 mg_{Ir}/cm^2, indicating that the excessive thickness of CL is easy to lead to the decline of electronic conductivity. On the other hand, excessively low CL thickness can easily make PTL contact with the membrane during compression, which will also lead to a decrease in low electronic conductivity. Therefore, moderate CL thickness and Ir loading are needed to ensure the performance of the membrane electrode.

3. CONCLUSIONS

In conclusion, the polyol method and monolayer adsorption process of Ir on the surface of TiO_2 were used to prepare Ir/TiO_2, and the MEA with different anode loads was prepared by ultrasonic spraying in this work. According to the polarization curve, anatase TiO_2 was determined as a better substrate choice, and only an overpotential of 288 mV was required to reach a current density of 10 mA/cm^2, a value which was lower than that for the catalyst made of rutile TiO_2 (346 mV). Meanwhile, the mass activity of anatase TiO_2 was higher, which could reach 7.81 times that of rutile TiO_2. Compared with previous work, the Ir load of MEA prepared based on Ir/1-TiO_2 composite material had been reduced. Moreover, the test results of the single electrolytic cell showed that the system had low voltage loss and resistance with the Ir load in the range of 0.204−0.304 mg_{Ir}/cm^2. The material design method proposed in this paper could effectively reduce the operating cost of the PEMWE anode by reducing the load of precious metal. On the other hand, a suitable load range was given through a capacity-performance analysis, providing novel insight into the trade-off between performance and economy. This research has provided some valuable experience for the industrial development and practical application planning of electrolytic water splitting technology.

https://doi.org/10.1021/acsomega.4c02299
ACS Omega 2024, 9, 34482−34492

4. EXPERIMENTAL SECTION

4.1. Synthesis of Ir/TiO_2. The Ir/TiO_2 composite material was prepared by the polyol method. First, 20 mg of TiO_2 was dissolved in 20 mL of ethylene glycol, and the TiO_2 was completely dispersed by ultrasonic stirring for 1 h. Then, 18.05 mg of $IrCl_3$ was added while stirring for 30 min, and the reaction was performed at 180 °C for 3 h in an autoclave. After the reaction, the sample was put into 40 mL of 1.2 M sulfuric acid solution for acid washing. Finally, Ir/TiO_2 sample was completely prepared after filtration, washing three times with water, and drying in a vacuum drying oven at 80 °C overnight.

4.2. Synthesis of Catalyst Slurry. 50 mg of catalyst was accurately weighed and placed in a beaker. Then, 10 mL of ethanol solution was slowly added and the beaker was ultrasonically dispersed in an ice bath for 1 h to ensure that the catalyst was completely dispersed in the ethanol solution. During the ultrasonic process, Nafion solution (20 wt %) with the same weight as the catalyst was slowly added, and ethanol solution was continued to make the catalyst content of the final slurry 3 mg/mL. Similarly, Pt/C (47.5%, TKK) catalyst was used for the cathode slurry and the final catalyst content was 2 mg_{Pt}/mL.

4.3. Synthesis of MEA. The vacuum adsorption platform of the Sono-Tek ultrasonic desktop spraying equipment was heated to 70 °C and stabilized for 1 h before spraying. The slurry was placed in the suction tube of the volume pump of the spraying equipment and ultrasonically sprayed onto the proton exchange membrane (Nafion 117 membrane, thickness = 0.18 mm) at a certain flow rate. The anode was with different spray amounts for comparison, and the cathode spray amount was about 4 mg_{Pt}/cm^2. The sample after spraying was labeled catalyst-coated membrane (CCM). The hot press was heated to 140 °C and stabilized for 30 min. The carbon paper was coated on the cathode and anode, respectively, and was consistent with CL shape. After that, the carbon paper was coated with a poly(tetrafluoroethylene) (PTFE) gasket. The sample was hot-pressed under 50 kg/cm^2 pressure for 2 min, then removed and cooled to room temperature, and the preparation of MEA was completed.

4.4. Electrolytic Cell Assembly. The cell was assembled in the order of positive terminal plate, insulating gasket, current collector, anode bipolar plate, anode porous transport layer, membrane electrode, cathode porous transport layer, cathode bipolar plate, current collector, insulating gasket, and negative terminal plate. And the cell was compressed uniformly with a fixed pressure.

Physical and electrochemical characterizations are provided in the Supporting Information.

■ ASSOCIATED CONTENT

Supporting Information

The Supporting Information is available free of charge at https://pubs.acs.org/doi/10.1021/acsomega.4c02299.

Phase characterization and electrochemical test methods; cell voltage loss analysis; N_2 adsorption−desorption isotherms; and monolayer adsorption hypothesis (PDF)

■ AUTHOR INFORMATION

Corresponding Author

Jie Zhang − *College of Chemical Engineering, Beijing University of Chemical Technology, Beijing 100029, China; Qingdao Chuangqi New Energy Catalysis Technology Co., Ltd., Qingdao 266199, China;* orcid.org/0000-0002-3059-1978; Email: zhangjie@mail.buct.edu.cn

Authors

Peng Huang − *China Coal Research Institute, Beijing 100013, China*

Xiao Xu − *College of Chemical Engineering, Beijing University of Chemical Technology, Beijing 100029, China*

Yashi Hao − *College of Chemical Engineering, Beijing University of Chemical Technology, Beijing 100029, China*

Hong Zhao − *College of Chemical Engineering, Beijing University of Chemical Technology, Beijing 100029, China;* orcid.org/0000-0003-2879-2321

Xin Liang − *College of Chemical Engineering, Beijing University of Chemical Technology, Beijing 100029, China;* orcid.org/0000-0001-9268-0194

Zuobo Yang − *College of Chemical Engineering, Beijing University of Chemical Technology, Beijing 100029, China*

Jimmy Yun − *Qingdao Chuangqi New Energy Catalysis Technology Co., Ltd., Qingdao 266199, China; School of Chemical Engineering, The University of New South Wales, Sydney, NSW 2052, Australia*

Complete contact information is available at: https://pubs.acs.org/10.1021/acsomega.4c02299

Notes

The authors declare no competing financial interest.

■ ACKNOWLEDGMENTS

The authors thank the National Key Research and Development Program of China (2023YFB4004705) and the special funds for technology entrepreneurship of TD Technology Co. Ltd. (2022-2-TD-MS001) for supporting this work.

■ REFERENCES

(1) Zhang, S.; Chen, W. China's Energy Transition Pathway in a Carbon Neutral Vision. *Engineering* **2022**, *14*, 64−76.

(2) Quinson, J. Iridium and IrO_x nanoparticles: an overview and review of syntheses and applications. *Adv. Colloid Interface Sci.* **2022**, *303*, No. 102643.

(3) Fan, M.; Liang, X.; Chen, H.; Zou, X. Low-iridium electrocatalysts for acidic oxygen evolution. *Dalton Trans.* **2020**, *49* (44), 15568−15573.

(4) Jiang, G.; Yu, H.; Li, Y.; Yao, D.; Chi, J.; Sun, S.; Shao, Z. Low-Loading and Highly Stable Membrane Electrode Based on an Ir@WOxNR Ordered Array for PEM Water Electrolysis. *ACS Appl. Mater. Interfaces* **2021**, *13* (13), 15073−15082.

(5) Djara, R.; Lacour, M.-A.; Merzouki, A.; Cambedouzou, J.; Cornu, D.; Tingry, S.; Holade, Y. Iridium and Ruthenium Modified Polyaniline Polymer Leads to Nanostructured Electrocatalysts with High Performance Regarding Water Splitting. *Polymers* **2021**, *13* (2), No. 190, DOI: 10.3390/polym13020190.

(6) Li, Y.; Zhu, Y.-Q.; Xin, W.; Hong, S.; Zhao, X.; Yan, H.; Xu, S. Interlayer confinement synthesis of Ir nanodots/dual carbon as an electrocatalyst for overall water splitting. *J. Mater. Chem. A* **2021**, *9* (7), 4176−4183.

(7) Zhang, K.; Mai, W.; Li, J.; Wang, H.; Li, G.; Hu, W. Highly scattered Ir oxides on TiN as an efficient oxygen evolution reaction electrocatalyst in acidic media. *J. Mater. Sci.* **2020**, *55* (8), 3507−3520.

(8) Ledendecker, M.; Geiger, S.; Hengge, K.; Lim, J.; Cherevko, S.; Mingers, A. M.; Göhl, D.; Fortunato, G. V.; Jalalpoor, D.; Schüth, F.; Scheu, C.; Mayrhofer, K. J. J. Towards maximized utilization of iridium for the acidic oxygen evolution reaction. *Nano Res.* **2019**, *12* (9), 2275−2280.

(9) Singh, A. K.; Zhou, L.; Shinde, A.; Suram, S. K.; Montoya, J. H.; Winston, D.; Gregoire, J. M.; Persson, K. A. Electrochemical Stability of Metastable Materials. *Chem. Mater.* **2017**, *29* (23), 10159−10167.
(10) Quílez-Bermejo, J.; García-Dalí, S.; Daouli, A.; Zitolo, A.; Canevesi, R. L. S.; Emo, M.; Izquierdo, M. T.; Badawi, M.; Celzard, A.; Fierro, V. Advanced Design of Metal Nanoclusters and Single Atoms Embedded in C1N1-Derived Carbon Materials for ORR, HER, and OER. *Adv. Funct. Mater.* **2023**, *33* (21), No. 2300405.
(11) Wang, J.; Ciucci, F. In-situ synthesis of bimetallic phosphide with carbon tubes as an active electrocatalyst for oxygen evolution reaction. *Appl. Catal., B* **2019**, *254*, 292−299.
(12) Meier, J. C.; Galeano, C.; Katsounaros, I.; Topalov, A. A.; Kostka, A.; Schüth, F.; Mayrhofer, K. J. J. Degradation Mechanisms of Pt/C Fuel Cell Catalysts under Simulated Start−Stop Conditions. *ACS Catal.* **2012**, *2* (5), 832−843.
(13) Filimonenkov, I. S.; Bouillet, C.; Kéranguéven, G.; Simonov, P. A.; Tsirlina, G. A.; Savinova, E. R. Carbon materials as additives to the OER catalysts: RRDE study of carbon corrosion at high anodic potentials. *Electrochim. Acta* **2019**, *321*, No. 134657, DOI: 10.1016/j.electacta.2019.134657.
(14) Martínez-Séptimo, A.; Valenzuela, M. A.; Del Angel, P.; González-Huerta, R. d. G. $IrRuO_x/TiO_2$ a stable electrocatalyst for the oxygen evolution reaction in acidic media. *Int. J. Hydrogen Energy* **2021**, *46* (51), 25918−25928, DOI: 10.1016/j.ijhydene.2021.04.040.
(15) Wang, Z.; Zheng, Y.-R.; Chorkendorff, I.; Nørskov, J. K. Acid-Stable Oxides for Oxygen Electrocatalysis. *ACS Energy Lett.* **2020**, *5* (9), 2905−2908.
(16) Chen, Y. W.; Prange, J. D.; Dühnen, S.; Park, Y.; Gunji, M.; Chidsey, C. E. D.; McIntyre, P. C. Atomic layer-deposited tunnel oxide stabilizes silicon photoanodes for water oxidation. *Nat. Mater.* **2011**, *10* (7), 539−544.
(17) Hoffmeister, D.; Finger, S.; Fiedler, L.; Ma, T.-C.; Körner, A.; Zlatar, M.; Fritsch, B.; Witte-Bodnar, K.; Carl, S.; Götz, A.; Apeleo Zubiri, B.; Will, J.; Spiecker, E.; Cherevko, S.; Freiberg, A. T. S.; Mayrhofer, K. J. J.; Thiele, S.; Hutzler, A.; Van Pham, C. *Scalable Synthesis of TiO_2@IrO_x Core−Shell Catalyst for Proton Exchange Membrane Water Electrolysis with Low Iridium Loading*; ChemRxiv, 2024.
(18) Bernt, M.; Schramm, C.; Schröter, J.; Gebauer, C.; Byrknes, J.; Eickes, C.; Gasteiger, H. A. Effect of the IrO_x Conductivity on the Anode Electrode/Porous Transport Layer Interfacial Resistance in PEM Water Electrolyzers. *J. Electrochem. Soc.* **2021**, *168* (8), No. 084513.
(19) Pham, C. V.; Escalera-López, D.; Mayrhofer, K.; Cherevko, S.; Thiele, S. Essentials of High Performance Water Electrolyzers − From Catalyst Layer Materials to Electrode Engineering. *Adv. Energy. Mater.* **2021**, *11* (44), No. 2101998.
(20) Feng, Q.; Yuan, X. Z.; Liu, G.; Wei, B.; Zhang, Z.; Li, H.; Wang, H. A review of proton exchange membrane water electrolysis on degradation mechanisms and mitigation strategies. *J. Power Sources* **2017**, *366*, 33−55.
(21) Di Blasi, A.; Andaloro, L.; Siracusano, S.; Briguglio, N.; Brunaccini, G.; Stassi, A.; Aricò, A. S.; Antonucci, V. Evaluation of materials and components degradation of a PEM electrolyzer for marine applications. *Int. J. Hydrogen Energy* **2013**, *38* (18), 7612−7615.
(22) Frensch, S. H.; Fouda-Onana, F.; Serre, G.; Thoby, D.; Araya, S. S.; Kær, S. K. Influence of the operation mode on PEM water electrolysis degradation. *Int. J. Hydrogen Energy* **2019**, *44* (57), 29889−29898.
(23) Cheng, J.; Yang, J.; Kitano, S.; Juhasz, G.; Higashi, M.; Sadakiyo, M.; Kato, K.; Yoshioka, S.; Sugiyama, T.; Yamauchi, M.; Nakashima, N. Impact of Ir-Valence Control and Surface Nanostructure on Oxygen Evolution Reaction over a Highly Efficient Ir−TiO2 Nanorod Catalyst. *ACS Catal.* **2019**, *9* (8), 6974−6986.
(24) Schlicht, S.; Büttner, P.; Bachmann, J. Highly Active Ir/TiO2 Electrodes for the Oxygen Evolution Reaction Using Atomic Layer Deposition on Ordered Porous Substrates. *ACS Appl. Energy Mater.* **2019**, *2* (3), 2344−2349.
(25) Zhu, H.; Shen, M.; Wu, Y.; Li, X.; Hong, J.; Liu, B.; Wu, X.; Dong, L.; Chen, Y. Dispersion Behaviors of Molybdena on Titania (Rutile and/or Anatase). *J. Phys. Chem. B* **2005**, *109*, 11720−11726.
(26) Nguyen, C. T. K.; Tran, N. Q.; Le, T. A.; Lee, H. Covalently Bonded Ir(IV) on Conducted Blue TiO_2 for Efficient Electrocatalytic Oxygen Evolution Reaction in Acid Media. *Catalysts* **2021**, *11* (10), No. 1176, DOI: 10.3390/catal11101176.
(27) Zhao, S.; Xia, J.; Xia, Y.; Chen, J.; Du, D.; Yang, H.; Liu, J. Microstructure and Isothermal Oxidation of Ir−Rh Spark Plug Electrodes. *Materials* **2019**, *12* (19), No. 3226, DOI: 10.3390/ma12193226.
(28) Sun, Z.; Kim, J. H.; Zhao, Y.; Bijarbooneh, F.; Malgras, V.; Lee, Y.; Kang, Y.-M.; Dou, S. X. Rational Design of 3D Dendritic TiO_2 Nanostructures with Favorable Architectures. *J. Am. Chem. Soc.* **2011**, *133* (48), 19314−19317.
(29) Kang, Z.; Alia, S. M.; Carmo, M.; Bender, G. In-situ and in-operando analysis of voltage losses using sense wires for proton exchange membrane water electrolyzers. *J. Power Sources* **2021**, *481*, No. 229012.
(30) Chatenet, M.; Pollet, B. G.; Dekel, D. R.; Dionigi, F.; Deseure, J.; Millet, P.; Braatz, R. D.; Bazant, M. Z.; Eikerling, M.; Staffell, I.; Balcombe, P.; Shao-Horn, Y.; Schafer, H. Water electrolysis: from textbook knowledge to the latest scientific strategies and industrial developments. *Chem. Soc. Rev.* **2022**, *51* (11), 4583−4762.
(31) Mo, J.; Kang, Z.; Yang, G.; Retterer, S. T.; Cullen, D. A.; Toops, T. J.; Green, J. B.; Zhang, F.-Y. Thin liquid/gas diffusion layers for high-efficiency hydrogen production from water splitting. *Appl. Energy* **2016**, *177*, 817−822.
(32) Carmo, M.; Keeley, G. P.; Holtz, D.; Grube, T.; Robinius, M.; Müller, M.; Stolten, D. PEM water electrolysis: Innovative approaches towards catalyst separation, recovery and recycling. *Int. J. Hydrogen Energy* **2019**, *44* (7), 3450−3455.
(33) Bender, G.; Carmo, M.; Smolinka, T.; Gago, A.; Danilovic, N.; Mueller, M.; Ganci, F.; Fallisch, A.; Lettenmeier, P.; Friedrich, K. A.; Ayers, K.; Pivovar, B.; Mergel, J.; Stolten, D. Initial approaches in benchmarking and round robin testing for proton exchange membrane water electrolyzers. *Int. J. Hydrogen Energy* **2019**, *44* (18), 9174−9187.
(34) Jang, Y.; Seol, C.; Kim, S. M.; Jang, S. Investigation of the correlation effects of catalyst loading and ionomer content in an anode electrode on the performance of polymer electrode membrane water electrolysis. *Int. J. Hydrogen Energy* **2022**, *47* (42), 18229−18239.
(35) Zheng, T.; Sang, W.; He, Z.; Wei, Q.; Chen, B.; Li, H.; Cao, C.; Huang, R.; Yan, X.; Pan, B.; Zhou, S.; Zeng, J. Conductive Tungsten Oxide Nanosheets for Highly Efficient Hydrogen Evolution. *Nano Lett.* **2017**, *17* (12), 7968−7973.
(36) Ahn, C.-Y.; Kang, S. Y.; Choi, H. J.; Kim, O.-H.; Sung, Y.-E.; Cho, Y.-H. Effect of anode iridium oxide content on the electrochemical performance and resistance to cell reversal potential of polymer electrolyte membrane fuel cells. *Int. J. Hydrogen Energy* **2021**, *46* (27), 14713−14723.
(37) Carmo, M.; Fritz, D. L.; Mergel, J.; Stolten, D. A comprehensive review on PEM water electrolysis. *Int. J. Hydrogen Energy* **2013**, *38* (12), 4901−4934.
(38) Huang, J. Diffusion impedance of electroactive materials, electrolytic solutions and porous electrodes: Warburg impedance and beyond. *Electrochim. Acta* **2018**, *281*, 170−188.
(39) Yu, J.-W.; Jung, G.-b.; Su, Y.-J.; Yeh, C.-C.; Kan, M.-Y.; Lee, C.-Y.; Lai, C.-J. Proton exchange membrane water electrolysis system-membrane electrode assembly with additive. *Int. J. Hydrogen Energy* **2019**, *44* (30), 15721−15726.
(40) Jung, G.-B.; Chan, S.-H.; Lai, C.-J.; Yeh, C.-C.; Yu, J.-W. Innovative Membrane Electrode Assembly (MEA) Fabrication for Proton Exchange Membrane Water Electrolysis. *Energies* **2019**, *12* (21), No. 4218, DOI: 10.3390/en12214218.
(41) Ayers, K. High efficiency PEM water electrolysis: enabled by advanced catalysts, membranes, and processes. *Curr. Opin. Chem. Eng.* **2021**, *33*, No. 100719.

https://doi.org/10.1021/acsomega.4c02299
ACS Omega 2024, 9, 34482−34492

(42) Lee, C. H.; Lee, J. K.; Zhao, B.; Fahy, K. F.; Bazylak, A. Transient Gas Distribution in Porous Transport Layers of Polymer Electrolyte Membrane Electrolyzers. *J. Electrochem. Soc.* **2020**, *167* (2), No. 024508.
(43) Waraksa, C. C.; Chen, G.; Macdonald, D. D.; Mallouka, T. E. EIS Studies of Porous Oxygen Electrodes with Discrete Particles. *J. Electrochem. Soc.* **2003**, *150* (9), E429−E437.
(44) Özdemir, S. N.; Taymaz, I. Three-dimensional modeling of gas−liquid flow in the anode bipolar plate of a PEM electrolyzer. *J. Braz. Soc. Mech. Sci. Eng.* **2022**, *44* (8), No. 354, DOI: 10.1007/s40430-022-03664-y.
(45) Barbero, G.; Lelidis, I. Analysis of Warburg's impedance and its equivalent electric circuits. *Phys. Chem. Chem. Phys.* **2017**, *19* (36), 24934−24944.
(46) Kulikovsky, A. Why impedance of the gas diffusion layer in a PEM fuel cell differs from the Warburg finite-length impedance? *Electrochem. Commun.* **2017**, *84*, 28−31.

https://doi.org/10.1021/acsomega.4c02299
ACS Omega 2024, 9, 34482−34492